FISEVIER

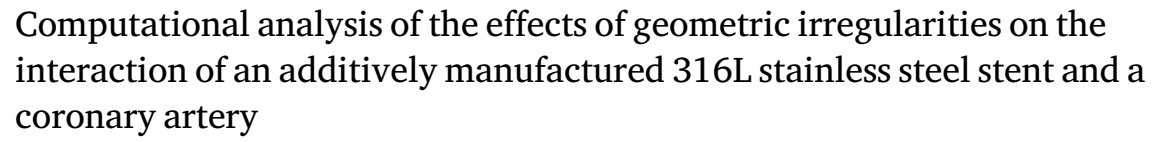
Contents lists available at ScienceDirect

Journal of the Mechanical Behavior of Biomedical Materials

journal homepage: www.elsevier.com/locate/jmbbm



Research paper



Lisa Wiesent a,b,*, Ashley Spear c, Aida Nonn a,b

- ^a Computational Mechanics and Materials Lab, Department of Mechanical Engineering, Ostbayerische Technische Hochschule (OTH) Regensburg, Regensburg, Germany
- b Technology Campus Neustadt a. d. Donau, Department of Mechanical Engineering, OTH Regensburg, Regensburg, Germany
- ^c Department of Mechanical Engineering, University of Utah, Salt Lake City, UT, USA

ARTICLE INFO

Keywords: Laser powder bed fusion (L-PBF) Cardiovascular stents Finite element analysis (FEA) Geometrical imperfections Stent-artery interaction

ABSTRACT

Customized additively manufactured (laser powder bed fused (L-PBF)) stents could improve the treatment of complex lesions by enhancing stent-artery conformity. However, geometric irregularities inherent for L-PBF stents are expected to influence not only their mechanical behavior but also their interaction with the artery. In this study, the influence of geometrical irregularities on stent-artery interaction is evaluated within a numerical framework. Thus, computed arterial stresses induced by a reconstructed L-PBF stent model are compared to those induced by the intended stent model (also representing a stent geometry obtained from conventional manufacturing processes) and a modified CAD stent model that accounts for the increased strut thickness inherent for L-PBF stents. It was found that, similar to conventionally manufactured stents, arterial stresses are initially related to the basic stent design/topology, with the highest stresses occurring at the indentations of the stent struts. Compared to the stent CAD model, the L-PBF stent induces distinctly higher and more maximum volume stresses within the plaque and the arterial wall. In return, the modified CAD model overestimates the arterial stresses induced by the L-PBF stent due to its homogeneously increased strut thickness and thus its homogeneously increased geometric stiffness compared with the L-PBF stent. Therefore, the L-PBF-induced geometric irregularities must be explicitly considered when evaluating the L-PBF stent-induced stresses because the intended stent CAD model underestimates the arterial stresses, whereas the modified CAD model overestimates them. The arterial stresses induced by the L-PBF stent were still within the range of values reported for conventional stents in literature, suggesting that the use of L-PBF stents is conceivable in principle. However, because geometric irregularities, such as protruding features from the stent surface, could potentially damage the artery or lead to premature stent failure, further improvement of L-PBF stents is essential.

1. Introduction

Advances in laser powder bed fusion (L-PBF) enable the production of filigree metallic lattice structures, making them increasingly attractive for biomedical applications (Mahmoud and Elbestawi, 2017; Parthasarathy et al., 2011). L-PBF is a powder based additive manufacturing (AM) technology, commonly known as selective laser melting (SLM). The extensive design possibilities of L-PBF in combination with near-net-shape production and an attractive strength-to-weight ratio enable the production of customized implants. By improving adherence and thus reducing inflammatory reactions, but also by enabling new

or simplifying existing treatment options, customized implants could improve the (long-term) clinical success. Although stent implantation is an established treatment method in cardiovascular therapy, the clinical outcome of this procedure could further benefit from customized L-PBF stents

Stents are filigree cylindrical, metallic lattice structures that are used for minimally invasive treatment of stenosis in patients with coronary heart disease. Despite advances in stenting and the introduction of drug-eluting stents (DES), neointimal hyperplasia with the associated re-vascularization after stent implantation, known as in-stent restenosis

Abbreviations: AM, additive manufacturing/additively manufactured; CAD, computer aided design; BD, build direction; CT, X-ray computed tomography; DES, drug-eluting stent; FEA, finite element analysis; FE, finite element; L-PBF, laser powder bed fusion/laser powder bed fused; ISR, in-stent restenosis

^{*} Correspondence to: Ostbayerische Technische Hochschule Regensburg, Fakultät Maschinenbau Galgenbergstraße 30, 93053 Regensburg, Germany. E-mail address: lisa.wiesent@oth-regensburg.de (L. Wiesent).

(ISR), remains a major clinical challenge (Grewe et al., 2000; Kastrati et al., 2001; Serruys et al., 2006; Kim and Dean, 2011). Neointimal hyperplasia is attributed to inflammatory reactions following stent-induced vascular wall injuries and to adverse changes in hemodynamics caused by implanted stent (Gyöngyösi et al., 2000; Wu et al., 2007; Chen et al., 2009; Stone et al., 2003; Timmins et al., 2011). Although studies have shown that the application of DES might reduce the ISR rate to less than 10%, this rate mainly applies to simple lesions in short straight vessels with homogeneous diameters but not necessarily to complex lesions (Htay and Liu, 2005; Serruys et al., 2006; Kim and Dean, 2011). In complex lesions (e.g. arterial bifurcations, long, tapered or curved vessels), ISR is associated with lower clinical success due to limited possibilities to achieve good stent-artery compliance (Kim and Dean, 2011; Htay and Liu, 2005; Latib and Colombo, 2008; Conway et al., 2012).

Since stent-artery interaction has a strong influence on the longterm clinical success of stent treatment, its analysis has become an integral part of stent research and development. To reduce the number of experimental studies as well as ethically questionable animal experiments, computational analyses of stent-artery interaction based on structural mechanics as well as fluid dynamics were established, enabling the identification of predictors for ISR (Timmins et al., 2008. 2011; Wu et al., 2007; Morlacchi et al., 2013; Prendergast et al., 2003; Auricchio et al., 2011; Wei et al., 2019). Within these simulations, a stent model is virtually expanded in an artery, and the interaction of the stent with the arterial wall or the influence of the stent on hemodynamics is assessed. The investigated artery models vary from simplified single-layer cylindrical artery models (Prendergast et al., 2003), to population-specific arterial models (Conway et al., 2012, 2014), to complex patient-specific models based on actual reconstruction of the artery (Auricchio et al., 2011; Morlacchi et al., 2013). Based on the computational analysis, stent design, diameter, and length, as well as vessel morphology (e.g. vessel curvature), were identified as critical factors for ISR, as these lead to high (local) vascular stress and/or negatively impact hemodynamics due to reduced stent-artery compliance (Timmins et al., 2008, 2011; Chen et al., 2009; Djukic et al., 2019; Wu et al., 2007). In complex lesions (e.g. long, curved arteries), the straightening effect of the stent, stent over-/undersizing and the overlapping of multiple stents have proven to be particularly critical (Timmins et al., 2008, 2011; Chen et al., 2009; Djukic et al., 2019; Wu et al., 2007; Morlacchi et al., 2013). Therefore, to address the remaining challenges of ISR, improvements in DES coatings, stent deployment strategies, and stent designs are still required (Lepor et al., 2002; De Beule et al., 2008; Serruys et al., 2006).

By enabling customized stents, L-PBF could contribute to the reduction of ISR in complex lesions, e.g. by providing curved, tapered or bifurcated stents. In combination with suitable balloon systems, customized stents could thus preserve the natural course of the vessel, avoid local over- or undersizing, and preclude multiple stent implantation. Research in the field of L-PBF stents is still quite nascent. In 2017, the first metallic L-PBF stents made from a cobalt-chrome (CoCr) alloy were presented (Demir and Previtali, 2017). Subsequent studies demonstrated the principle applicability of L-PBF stents made of CoCr and a novel biodegradable FeMnCS alloy by expanding them using a balloon catheter (Finazzi et al., 2019; Hufenbach et al., 2020). Recently, the compression and expansion behavior of 316L stainless steel L-PBF stents was investigated in a combined numerical and experimental study (Wiesent et al., 2020). These studies also showed that L-PBF stents exhibited geometric irregularities similar to L-PBF lattice structures, such as deviations in the cross-sectional shape of the struts, strut waviness, increased strut diameters and pores (Finazzi et al., 2020; Dong et al., 2018; Lei et al., 2019; Liu et al., 2017; Campoli et al., 2013; Karamooz Ravari and Kadkhodaei, 2015; Gonzalez and Nuno, 2016; Wiesent et al., 2020). It should be noted that the dimensions of coronary stent struts with diameters of $D_{strut} = 100 \mu m$ are within the range of the laser spot size of industry standard L-PBF machines (Finazzi et al.,

2020). Individual struts thus comprise only a single hatch, making the strut dimensions purely dependent on the resulting melt pool diameter. Therefore, the increased strut thicknesses observed with L-PBF stents can only partially be compensated for by reducing the strut thickness in the intended stent CAD model, or by subsequent surface treatment.

Although the stent surface can be smoothed by a surface treatment (e.g. electropolishing), it is currently not possible to compensate for all irregularities due to the small structural size of the stent struts (strut diameter of D \approx 100–200 µm), leaving an inhomogeneous surface with potential notches (Finazzi et al., 2020; Wiesent et al., 2020). During the actual stent application process, these irregularities might provoke excessive local stress concentrations within the deformed stent (Wiesent et al., 2020), as well as injuries to the arterial wall due to protruding features during stent implantation. The increased strut dimensions further lead to an increased initial outer stent diameter, which in turn increases the radial over-stretching of the artery during stent expansion and thus potentially leads to higher stent-induced arterial stresses. Quantitatively, this radial overstretching is described by the stent-to-artery deployment ratio R_{artery} , defined as the ratio of the outer diameter of the expanded stent to the initial inner arterial diameter, $R_{artery} = D_{o,stent_{exp}}/D_{i,artery_{init}}$. However, since stents are not in direct contact with the healthy blood vessel but serve to compress the plaque, it is not yet clear whether the geometric irregularities actually lead to higher stresses in the healthy vessel or merely to higher stresses in the atherosclerotic plaque. At this early stage of L-PBF stent development, the analysis of stent-artery interactions using elaborate and ethically questionable animal experiments can hardly be justified. However, numerical simulations can be leveraged to perform preliminary analyses and thus provide first insights into the basic applicability or necessary improvements of L-PBF stents.

In light of the above overview, the aim of this study is to analyze the effects of L-PBF process-related geometric irregularities, especially surface irregularities and increased strut thickness, on the stent-artery interaction by assessing stent-induced arterial stresses within a finite element analysis (FEA). Computational studies on stent-artery interaction are commonly based on a computer aided design (CAD) stent model, as this is almost identical to the shape of conventionally manufactured stents. In these studies, it was found that the stent-induced arterial stresses are mainly related to the primary stent topology/design (Prendergast et al., 2003; Morlacchi et al., 2013; Auricchio et al., 2011; Wu et al., 2007; Timmins et al., 2008, 2011; Wei et al., 2019; Schiavone et al., 2014; Conway et al., 2012). However, this approach is not sufficient to investigate the influence of L-PBF process-related irregularities; rather, the geometric irregularities must be explicitly represented within the stent models, and the arterial stresses induced by these irregularities must be distinguished from those induced by the primary stent design/topology. To evaluate the impact of both, the surface irregularities and increased strut thickness, three stent models are investigated: the first stent based on the original CAD design, the second with the increased strut dimensions, and the third based on the reconstruction of an actual L-PBF stent. Each stent model is virtually expanded within one artery model and subsequently the stent-induced arterial stresses are evaluated.

2. Methods

2.1. Stent model

The three stent models investigated in this work compose: (i) a stent model (stent $_{CAD}$) based on the original intended CAD design, (ii) a stent model (stent $_{CAD/L-PBF}$) based on a modification of the original CAD design to account for the increased strut dimensions inherent to L-PBF stents, and (iii) a stent model (stent $_{L-PBF}$) based on the reconstruction of an actual L-PBF stent from X-ray computed tomography (CT) data. The three stent models are all based on the same stent design adopted from a previous study (Wiesent et al.,

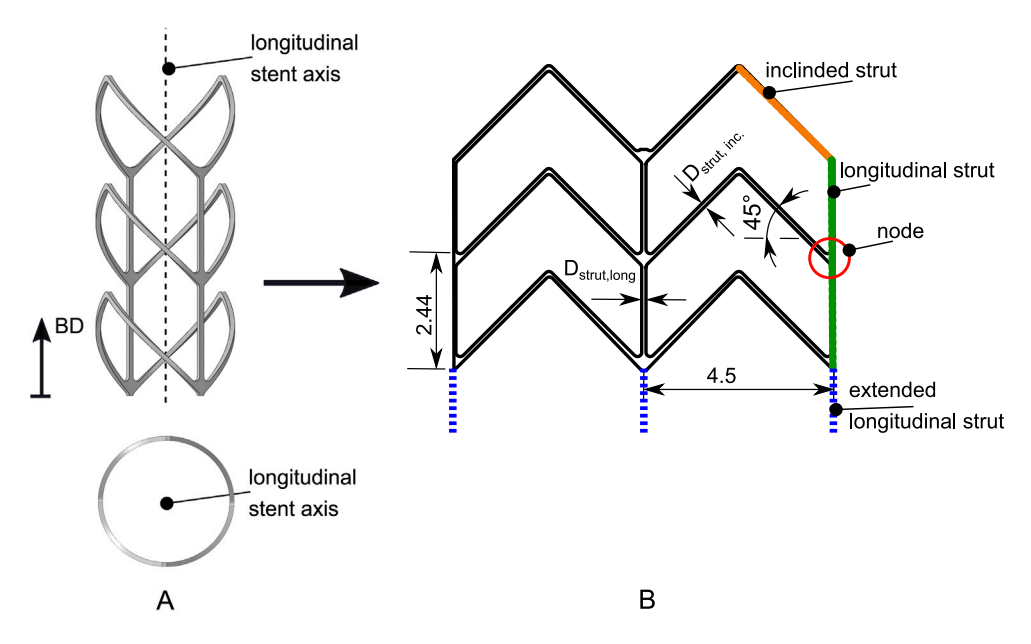


Fig. 1. Intended stent design. A: 3D stent CAD model in a rotated isometric view (top) and the front view (bottom). B: Flat projection of the intended stent design illustrating the basic dimensions of the stent unit cell model, given in mm. The longitudinal and inclined struts are highlighted in green and orange. The extended longitudinal struts that serve to support the stent on the built platform are illustrated by the dashed blue lines. The strut node and the tip of the stent spikes are further marked with red circles, respectively. The later build direction (BD) is indicated by the arrow.

Source: Adapted from Wiesent et al. (2020).

2020). Once heat- and surface-treated, L-PBF stents based on this design were found to exhibit comparable radial strengths and expansion behavior to conventionally manufactured stents (Wiesent et al., 2020). For computational efficiency, the stent length was reduced to two unit cells along the longitudinal axis in the present study (Fig. 1). This model reduction strategy was previously applied in Balossino et al. (2008). The reduction in stent length is justified as this study does not investigate the transient expansion behavior but rather the interaction of the expanded stent and its geometrical irregularities with the arterial wall. Nevertheless, in this way a statistical variance of geometrical irregularities of four longitudinal and twelve inclined struts (six peaks) can be considered while keeping the computational time within reasonable limits.

For stent $_{L-PBF}$ rather round and elliptical strut cross-sections with an average equivalent circular diameter of $\bar{D}_{strut,long}=130~\mu m$ and $\bar{D}_{strut,inc}=200~\mu m$ were determined for the longitudinal and inclined struts, respectively (Wiesent et al., 2020). Thus, to generate stent $_{CAD/L-PBF}$, the strut widths of the longitudinal and inclined struts were increased to $w_{strut,long}=130~\mu m$ and $w_{strut,inc}=220~\mu m$, respectively. The thickness of the struts was uniformly increased to $t_{strut}=150~\mu m$ to achieve equivalent spherical diameter compared to the L-PBF stent. To further account for the rather round/elliptical cross-sectional shape of L-PBF stent struts, the edges of stent $_{CAD/L-PBF}$ were rounded by a radius of $R=60~\mu m$. The reconstructed stent $_{L-PBF}$ model is adopted from a previous study (Wiesent et al., 2020). In the following, a brief overview of the L-PBF manufacturing process, post-processing steps, and the model reconstruction is provided. For a more detailed description, the reader is referred to Wiesent et al. (2020).

The L-PBF stent was made from gas-atomized 316L stainless steel powder with a particle diameter of $D_{powder}=15$ to 45 μ m (LPW, Rundkorn, United Kingdom) on a SLM 250 machine (SLM Solutions Group AG, Lübeck, Germany) equipped with a 400 W Yb-fiber-laser with the following process parameters: laser power of P=350 W, scanning velocity of v=700 mm/s, focus position of 0, layer thickness of $t_{layer}=30$ μ m. The longitudinal connecting struts of the stents were aligned parallel to the build direction. To prevent the filigree stents from fusing with the build platform, the longitudinal connection struts were extended beyond the actual stent geometry to support the stents

on the build platform (Fig. 1, blue dashed lines). Upon completion, the stent is removed from the build platform by cutting this extension. Thereupon, the stent is subjected to post-processing steps such as heat treatment (1050 °C, 1 h, cooled in oven) and electropolishing (electrolyte Polygrat E 268, 85 °C, 3.8 V, 5.5–6 A, 4 min). In the previous study (Wiesent et al., 2020), it was found that by applying these post-processing steps, an expansion behavior of the L-PBF 316L stent comparable to conventional stents can be achieved. The final stent configuration was then visualized using X-ray computed tomography (CT) (Phoenix v|tome|xs 240–180, GE Sensing Inspection Technologies, Hürth, Germany; 90 kV, 390 μ A, voxel size 8.5 μ m) and the stent geometry was extracted from the X-ray CT data using the 3-dimensional (3D) segmentation software Simpleware ScanIP (Synopsis, Mountain View, California, USA). Finally, the stent model was reduced to two unit cells along the longitudinal stent axis using the cropping tool.

The basic dimensions of the respective stent model are given in Table 1 with the geometrical deviations between ${\rm stent}_{CAD}$ and ${\rm stent}_{L-PBF}$ being attributed to the L-PBF process-related geometrical irregularities. Because the morphology of a conventional laser-cut stent is nearly identical to the CAD model, ${\rm stent}_{CAD}$ also represents a stent from conventional stent manufacturing. By comparing the vascular responses to expansion of ${\rm stent}_{L-PBF}$ and ${\rm stent}_{CAD}$, the arterial stresses induced by the primary stent design can be distinguished from those induced by the overall process-related irregularities (surface irregularities, increased strut dimensions). Stent_{L-PBF} and ${\rm stent}_{CAD/L-PBF}$ have comparable strut dimensions, and thus induce similar stent-to-artery deployment ratios. Therefore, by comparing the arterial stresses induced by ${\rm stent}_{L-PBF}$ and ${\rm stent}_{CAD/L-PBF}$, the effect of surface irregularities can be evaluated in isolation, excluding the influence of increased strut dimensions.

To minimize any mesh-related influence on the stent-induced arterial stresses, care was taken to discretize all three stents with a comparable mesh. Thus, stent $_{CAD}$ was discretized by 122 967, stent $_{CAD/L-PBF}$ by 219 110 and stent $_{L-PBF}$ by 228 874 linear tetrahedral elements (Abaqus type C3D4) with a mean edge length of 0.03 mm (Fig. 2A).

The material properties of the L-PBF heat treated 316L stent are taken from a previous study (Wiesent et al., 2020). The elastic material properties are described by a Young's modulus of $E=193\,$ GPa and

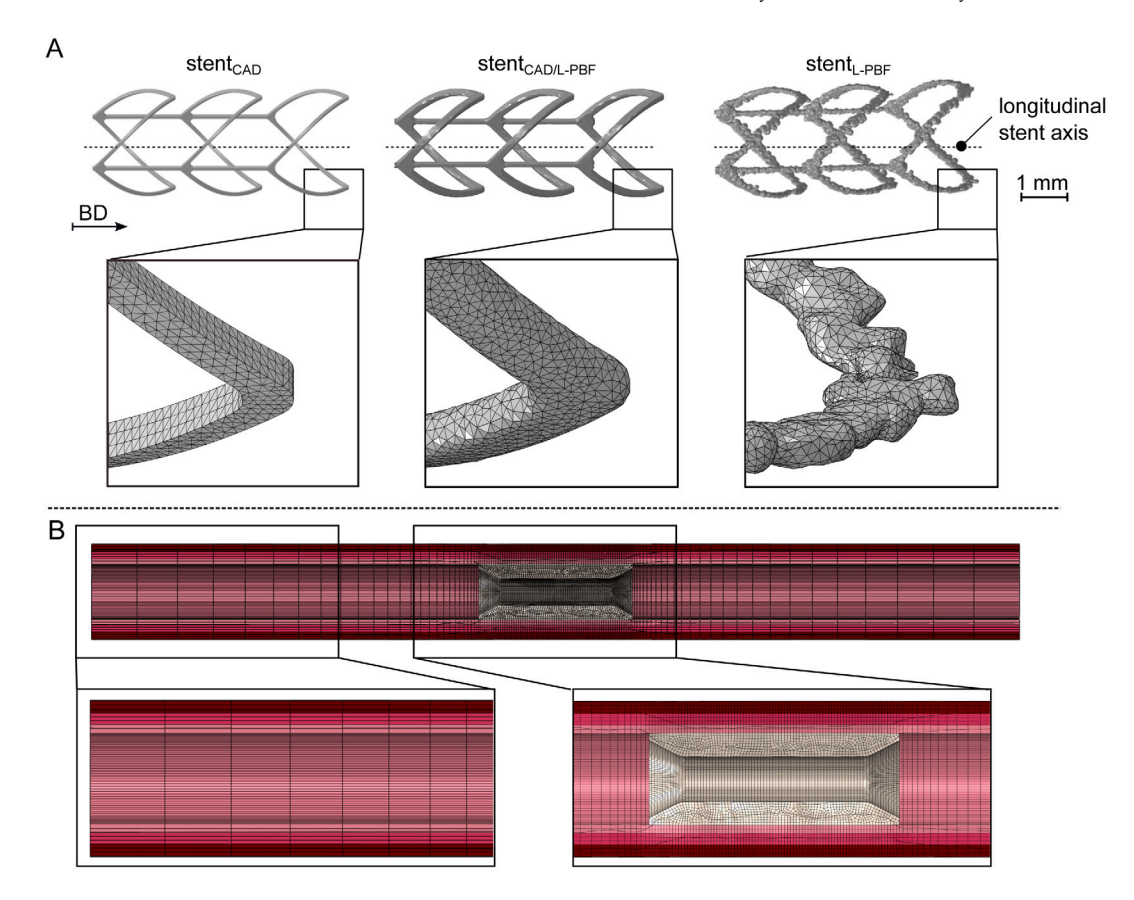


Fig. 2. Investigated stent models and artery model in this study with magnified view of mesh. A: stent models with (from left to right) the intended computed aided design stent $_{CAD}$ model, the modified CAD stent model stent $_{CAD/L-PBF}$ with increased strut thickness to account for the increased strut diameter inherent for L-PBF stents, and the reconstructed stent $_{L-PBF}$ model based on laser powder bed fused, heat-treated, and electropolished stent with the build direction (BD) indicated by the arrow. B: artery model with mesh size increasing from the stenotic area towards the free ends of the artery.

Table 1 Average basic dimensions of the stent models including the outer stent diameter ($\bar{D}_{o,steml_{int}}$), the stent length (\bar{l}_{steml}), and the average strut cross-sectional area (\bar{A}_{strut}) of the inclined and longitudinal struts.

	$ar{D}_{o,stent_{init}}$ (mm)	\bar{l}_{stent} (mm)	$\bar{A}_{strut,long}$ (mm ²)	$\bar{A}_{strut,inc}, (mm^2)$
$stent_{\mathit{CAD}}$	3.00	7.23	0.01 ^a	0.01 ^a
$stent_{CAD/L-PBF}$	3.20	7.78	≈ 0.014 ^b	$\approx 0.030^{\text{b}}$
$stent_{L-PBF}$	3.20	7.65	≈ 0.013 ^b	≈ 0.031 ^b

^astent_{CAD} exhibits an quadratic cross-sectional area for the longitudinal and inclined struts, respectively. The average strut cross-sectional area was thus calculated using the equivalent circular diameter of the struts.

a Poisson's ratio of $\nu=0.3$ (Nandishwarsteel, 2010). The inelastic constitutive behavior is described by a von Mises plasticity material model with isotropic hardening. The flow curve is given in Fig. 3 and can be described by a power-law hardening expression, the so-called Hollomon equation, $(\bar{\sigma}(\bar{\epsilon}^{pl})=A\cdot(\bar{\epsilon}^{pl})^n)$ with the strength coefficient of A = 1157 MPa and the strain hardening exponent of n = 0.35. The yield strength was determined to be $\sigma_y=117$ MPa. The density of L-PBF 316L was assumed to be 8.0 g/cm³ (Nandishwarsteel, 2010). To isolate the impact of geometrical differences, the same material model is used for all stent models.

2.2. Artery model

The stenotic artery is modeled as a straight cylinder with an arterial wall thickness of $t_{artery}=0.9$ mm, an outer diameter of $D_{o,artery_{init}}=4.5$ mm and a length of $l_{artery}=40$ mm (Holzapfel et al., 2005; He et al., 2020). The three layers of the artery (i.e., intima, media, and adventitia) are modeled with thicknesses of $t_{intima}=0.24$ mm, $t_{media}=0.32$ mm, and $t_{adventitia}=0.34$ mm (Holzapfel et al., 2005). The stenotic

plaque is considered symmetric with a length of $l_{plaque} = 6.6$ mm and a thickness of $t_{plaque} = 0.675$ mm, thus representing a stenosis by 50% in terms of arterial lumen reduction (i.a. an inner diameter of $D_{i,plaque} = 1.35$ mm), and aligned symmetrically at the center of the longitudinal arterial axis. The artery and the plaque are modeled with 209 760 eight-node linear brick elements with reduced integration and enhanced hourglass control of type C3D8R. The plaque was meshed with 84 816 elements with an average element size of 0.08 mm and 10 elements in the radial direction. The artery is meshed with 124 944 elements. In the radial direction, the intima is meshed with two rows of elements and the media and adventitia with three rows of elements, respectively. In the longitudinal direction, the element size of the arterial layers in the area of the stenosis, as well as the contact area of the stent, is 0.08 mm. For reasons of computational efficiency, the element size then successively increases to 2.0 mm towards the free ends of the arteries, similar to He et al. (2020) (Fig. 2B). Layerspecific material properties are assigned to the arterial wall layer and the plaque assuming, isotropic and hyperelastic material. The simplifying assumption of isotropic material properties can be justified by

 $^{^{\}rm b}$ stent_{L-PBF} and stent_{CAD/L-PBF} exhibits a more round and more elliptical cross-sectional area for the longitudinal and inclined struts, respectively. The average strut cross-sectional area was thus calculated using the equivalent circular diameter of the struts.

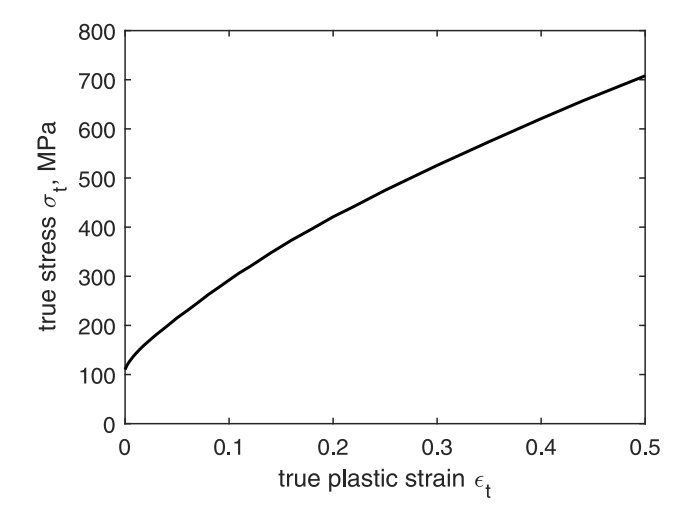


Fig. 3. Flow curve to describe the plastic material behavior of the laser powder bed fused 316L stent in the heat treated condition, determined in a previous study by the authors (Wiesent et al., 2020).

the fact that during stent implantation the circumferential mechanical properties of the artery are dominant (Zahedmanesh and Lally, 2009). The individual arterial layers are described by a third order Ogden hyperelastic constitutive equation (Ogden, 1972), which is described as:

$$W = \sum_{i=1}^{3} \frac{2\mu_i}{\alpha_i} \left(\bar{\lambda}_1^{\alpha_i} + \bar{\lambda}_2^{\alpha_i} + \bar{\lambda}_3^{\alpha_i} - 3 \right) + \sum_{n=1}^{3} \frac{1}{D_i} (J - 1)^{2i}, \tag{1}$$

where $\bar{\lambda}_i$ are the deviatoric principle stretches, J is the elastic volume strain, and μ_i , α_i , and D_i are hyperelastic constants. The values of the hyperelastic constants of the respective arterial layers are given in Table 2. These are adapted from Zahedmanesh and Lally (2009) who fitted these values based on the experimental data of Holzapfel et al. (2005) and Loree et al. (1994) of the arterial layers and the atherosclerotic plaque, respectively. The density of the plaque was taken from Rahdert et al. (1999) with a value of 1.45 g/cm³. The density of the individual arterial layers was considered homogeneous. All three vascular layers were therefore assigned a density value of 1.1 g/cm³ based on the density value of blood vessels in the IT'IS database (Hasgall et al., 2018).

2.3. Boundary conditions

To simulate stent crimping and expansion within the artery, the methodology described and validated in Grogan et al. (2012) and Wiesent et al. (2019) is implemented. Thus, within the FEA, a displacement-controlled approach is used that considers two loading scenarios: (i) stent crimping and (ii) stent deployment within the artery. The basic model set-up and boundary conditions are illustrated in Fig. 4. This approach has proven to be numerically efficient to evaluate the final expanded stent shape and was therefore specifically selected to evaluate the analysis of the effects of geometric irregularities on stent-artery interaction (Grogan et al., 2012; Wiesent et al., 2019). Simulation of stent crimping is accomplished by reducing the diameter of a semi-rigid crimping cylinder from $D_{c.cyl} = 4.0$ to 1.2 mm using a radial displacement boundary condition $\mathbf{u}_{r,crimp}$ and initiating contact between the crimping cylinder and the stent. During crimping, the rigid expansion cylinder with a diameter of $D_{cat} = 0.8$ mm is coaxially located inside the stent providing a kinematic limitation against crimping similar to the balloon catheter in reality. Once the final crimping diameter is reached, the crimping cylinder is retracted to account for elastic stent recoil.

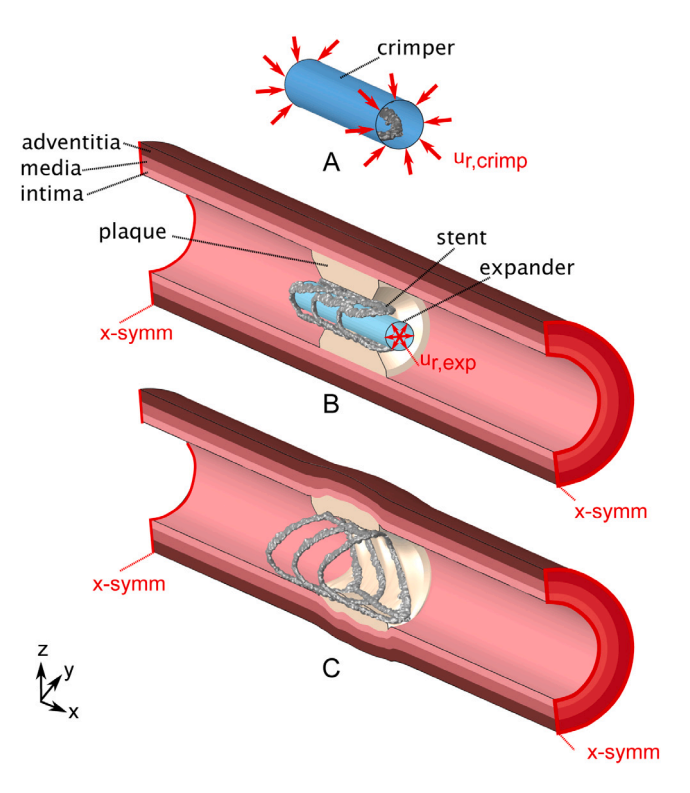


Fig. 4. Simulation set-up and the boundary conditions during A: stent crimping and B: stent expansion within the artery model and C: stent expanded within the artery.

Stent expansion within the artery is achieved by increasing the diameter of the expansion cylinder from $D_{e,cyl}=0.8$ to 2.6 mm by a radial displacement boundary condition $\mathbf{u}_{r,exp}$ and initiating contact between the stent and the expansion cylinder, the stent and the artery, as well as the expansion cylinder and the artery. The artery is constrained at both ends using symmetry boundary conditions in axial direction.

2.4. Numerical aspects

For the FEA, the finite element solver Abaqus/Explicit 2019 (Dassault Systèmes, Vèlizy-Villacoublay, France) is used. Care is taken to ensure that inertial effects do not become dominant by monitoring the ratio of internal to kinetic energy throughout the simulation process and ensuring that this ratio does not exceed a critical value of 5% during most of the simulation. Stent crimping and expansion was achieved within 0.01 s with a target time increment of 1×10^{-8} s adjusted via semi-automatic mass scaling. Therefore, the individual stable time increment of every single element is examined every 10 000 increments throughout the entire simulation steps. If the stable time increment of individual elements is below the target time, the mass of these critical elements is automatically (independently) scaled until the target time increment is reached (Dassault Systemes, 2013). Contact is invoked using the general contact algorithm (penalty method) in Abaqus/Explicit. All contacts within the model were considered frictionless (Zahedmanesh and Lally, 2009; Wei et al., 2019; Conway et al., 2012).

3. Results and discussion

The stent design/topology, strut dimensions, and L-PBF process-related geometric irregularities have been identified as critical factors of L-PBF stent-artery interaction. The shape and dimension of the expanded stent models within the arterial model, as well as the associated stent-to-artery deployment ratios, are presented and discussed first (Fig. 5, Table 3). Subsequently, the stent-induced arterial stresses

Table 2

Hyperelastic constants of the Ogden model used to describe the mechanical behavior of the arterial layers and the plaque.
Source: Adopted from Zahedmanesh and Lally (2009)

Material	μ ₁ (MPa)	μ ₂ (MPa)	μ ₃ (MPa)	α_1	α_2	α_3	D_1	D_2	D_3
Intima	7.04	4.23	2.85	24.48	25.00	23.54	8.95×10^{-7}	0	0
Media	-1.23	0.79	0.45	16.59	16.65	16.50	5.31×10^{-6}	0	0
Adventitia	-1.28	0.85	0.44	24.63	25.00	23.84	4.67×10^{-6}	0	0
Plaque	0.94	-	-	8.17	_	-	4.30×10^{-7}	0	0

Table 3

Predicted average expanded outer stent diameter $(\bar{D}_{o,stent})$ and radial arterial stretch ratio (R_{artery}) of the idealized stent model (stent_{CAD}), the modified CAD model (stent_{CAD/L-PBF}), and the actual laser powder bed fused stent model (stent_{L-PBF}) at maximum expansion (index: exp) and after recoil (index: rec). The arterial stretch ratio (R_{artery}) was calculated as the ratio of maximum expanded/recoiled outer stent diameter $\bar{D}_{o,stent}$ to the initial inner arterial diameter of $D_{t,artery_{total}} = 2.7$ mm. Moreover, the value of the stented artery recoil (RC) is further provided.

	$\bar{D}_{o,stent_{exp}}$ (mm)	$R_{artery_{exp}}$	$\bar{D}_{o,stent_{rec}}$ (mm)	$R_{artery_{rec}}$	RC (%)
$stent_{CAD}$	2.77	1.03	2.39	0.89	13.8
$stent_{CAD/L-PBF}$	3.10	1.15	2.65	0.98	14.5
$stent_{L-PBF}$	3.05	1.13	2.61	0.97	14.4

are presented and discussed in terms of the overall arterial stress distribution (Figs. 6, 7, Table 4). Finally, the strain distribution within the stents (Fig. 8) is presented and discussed with respect to possible damage and the associated effect on L-PBF stent-artery interaction.

3.1. Expanded stent shapes

The average outer stent diameter at maximum expansion and the associated stent-to-artery deployment ratios are provided in Table 3. For conventionally manufactured stents, stent-to-artery deployment ratios of $R_{artery} = 1.0$ to 1.2 were reported (Kurata et al., 2018; Ijsselmuiden et al., 2003). As the stent-to-artery deployment ratios of all three investigated stent models fall within this range, a comparison of the determined stent-induced arterial stresses with studies in the literature is justified (Table 3). Stent $_{CAD}$ exhibits the smallest expanded diameter and thus the lowest stent-to-artery deployment ratio, which is reduced by about 9%-10% compared to stent_{CAD/L-PBF} and stent_{L-PBF}. This is not surprising given the smaller dimensions of the struts of stent_{CAD} and hence the reduced initial outer stent diameter compared to the other stent models (Fig. 1). Stent_{CAD/L-PBF} exhibits the largest maximum expanded stent diameter and thus the highest stent-to-artery deployment ratio. However, compared to the stent $_{L-PBF}$, its stent-toartery deployment ratio is only increased by 1.7 and 1.4% at maximum stent expansion and after recoil, respectively. The discrepancy between the modified CAD model (stent $_{CAD/L-PBF}$) and the reconstructed model (stent $_{L-PBF}$) is attributed to L-PBF process-related geometric inhomogeneities, such as strut waviness and inhomogeneous strut diameters, which result in locally larger or smaller stent diameters. Geometric surface irregularities are not depicted within stent $_{CAD/L-PBF}$, as its modifications only accounted for the uniformly increased strut dimensions. Nevertheless, $stent_{CAD/L-PBF}$ still provides a good approximation of the final expanded stent diameter of stent L_{-PBF} . Thus, $stent_{CAD/L-PBF}$ and $stent_{L-PBF}$ induce nearly comparable stent-toartery ratios, allowing for the isolated assessment of the influence of process-related irregularities on arterial stresses, independent of the increased stent thickness.

Radial recoil values are in the range of RC = 14% for all three stent models, higher than conventionally manufactured stents (e.g., Lapp, 2019: RC = 1-4%), but still within the range of other studies in the literature (e.g. Capelli et al., 2009: RC = 14-42%, Conway et al., 2012: RC = 7-20%.) Stent area coverage is an further important indicator of stent-artery interaction. The area coverage is primarily related to the stent topology/design and is thus similar for all three stent models. The investigated stent design has a very low area coverage. With

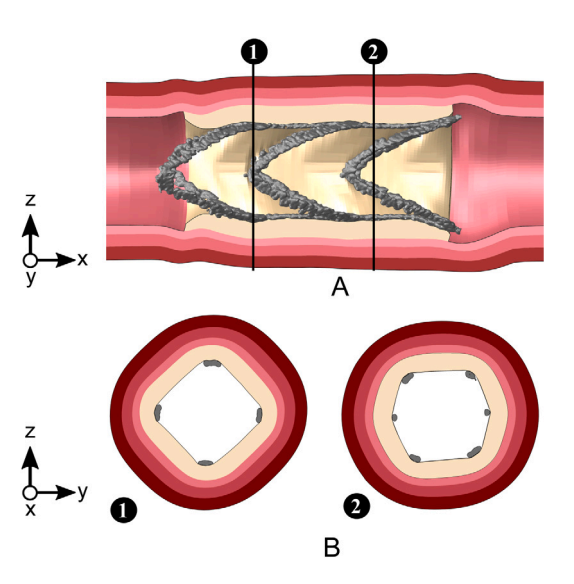


Fig. 5. Inhomogeneous dilation of the artery after stent expansion along the longitudinal stent axis. A: Expanded stent $_{L-PBF}$ within the artery highlighting the location of the sections. B: Sectional views in the yz-plane: ① Section across the tip of the stent spikes with four strut cross-sections dilating the artery; ② Section across the area between the node and the stent spikes with six strut cross-sections dilating the artery.

an outer surface area of $A_{o,stent}=3.79~{\rm mm^2}$, stent_{CAD} has an area coverage of approximately 6.1% for an equivalent enclosed cylinder area of $A_{eq,cyl}=61.9~{\rm mm^2}.^1$ Conventional stent designs, however, typically have an area coverage of approximately 12 to 15% (Lapp, 2019). The low area coverage, in combination with only two unit cells across the stent circumferential directions, causes an inhomogeneous angular dilation of the artery as well as local tissue prolapse through the interstitial areas of the stent unit cells (Fig. 5). Consequently, the artery is locally dilated by either four, or six strut cross-sections, resulting in an either square, or hexagonal dilatation of the artery.

In this study, the investigated L-PBF stent design was chosen to meet the requirements of L-PBF of filigree structures (i.e. without support structures Finazzi et al., 2019) and to be expandable by means of a balloon catheter; it was not intended to provide an optimized L-PBF stent design. Rather, the purpose of this comparative study was to demonstrate the influence of morphological irregularities associated with L-PBF on stent-artery interaction. Furthermore, one should note that in contrast to macroscopic L-PBF components, the design possibilities of filigree L-PBF structures are still very limited and subject to certain design guidelines, which only allow for a simpler self-supporting stent design (Finazzi et al., 2019). However, building on the results of this study, in addition to the manufacturability and expandability of L-PBF stents, stent-artery interactions need to be considered in the early stent design development stage. Nevertheless, regardless of the stent design chosen, this study is the first to analyze the influence of process-related irregularities of L-PBF stents on arterial stresses.

¹ $A_{eq,cyl} = D_{o,stent_{exp}} \cdot \pi \cdot l_{stent}$; with $D_{o,stent_{exp}} = 2.39$ mm and l_{stent} for stent_{CAD}

3.2. Stent-induced arterial stresses

Contour plots of the von Mises stress (σ_{vM}) of the respective arterial layers at maximum expansion and after recoil are shown in Fig. 6. The maximum and mean values of the stent-induced stresses within the atherosclerotic plaque and within the different layers of the stenosed part of the artery are further listed in Table 4. The mean arterial stresses were determined in the area of the stenosed artery. Thus, an artificial reduction of the arterial stresses due to the low stresses in the unloaded free area of the artery is avoided. In order to evaluate the stent-induced stresses in the intima and plaque in more detail, Fig. 7 shows an histogram of the stress volumes after stent recoil. Analogous to the indication of mean arterial stresses, this evaluation refers to the stenosed area of the intima. In this way, the percentages of the intima and plaque subjected to high and low stresses, respectively, can be evaluated to further analyze the effect of increased strut thickness and L-PBF process-related geometric irregularities.

Similar to conventionally manufactured stents, the location and magnitude of stent-induced arterial stresses are highly dependent on the stent design, with the highest arterial stresses occurring in the region of the strut indentations, and in particular at the U-bends/spikes of the stent (Wei et al., 2019; Schiavone et al., 2014). In the present study, high arterial stress is also observed in the area between the inclined struts. This may be attributed to the inhomogeneous radial expansion of the artery over the stent length due to the chosen stent design (see Fig. 5). Thus, at the stent spikes, the artery is expanded by four struts, stretching it into a square. Beyond the stent spikes, the artery is then dilated by six struts. Therefore, it is likely that significant arterial stresses will be generated in the transition region between the four- and six-strut expansion areas due to an abrupt change in the local artery deformation. Consequently, inhomogeneous expansion of the artery along the stent length should be considered critical and avoided in the development of further stent designs. The arterial stresses with $\sigma_{vM} > 0.2$ MPa occur exclusively in the intima and plaque (Fig. 6, Table 4). The stent-induced stresses within the media and adventitia have maximum values of $\sigma_{vM,max} < 0.059$ MPa for stent_{L-PBF} , $\sigma_{vM,max} < 0.065$ MPa for $\text{stent}_{CAD/L-PBF}$, and $\sigma_{vM,max} < 0.065$ 0.034 MPa for stent_{CAD} (Table 4b). Thus, regardless of the respective stent model, the stent-induced stresses in the media and adventitia are negligible compared to the stresses in the plaque and intima. Therefore, a more detailed analysis of the stress distribution in the media and adventitia is omitted.

At maximum stent expansion, the maximum von Mises stress in the plaque is $\sigma_{vM,max}=7.1$ MPa for stent $_{CAD}$, and $\sigma_{vM,max}=12.7/12.4$ MPa for stent $_{CAD/L-PBF}$ and stent $_{L-PBF}$, respectively. In the intima, the maximum von Mises stresses is $\sigma_{vM,max}=2.1$ MPa for stent $_{CAD}$ and $\sigma_{vM,max}=5.9/5.2$ MPa for stent $_{CAD/L-PBF}$ and stent $_{L-PBF}$, respectively. Numerical studies in the literature have shown arterial stresses at maximal stent expansion in the range of $\sigma_{vM}=1.2$ to 11 MPa (Schiavone et al., 2014; Wei et al., 2019; Morlacchi et al., 2013; Zahedmanesh and Lally, 2009). Thus, all three stent models are in the range of conventionally manufactured stents.

At maximal stent expansion, a high proportion of the intima and a comparable low portion of the plaque is subjected to stresses of $\sigma_{vM}>0.5$ MPa for all stent models. This can be attributed to the increased stiffness of the intima compared to the plaque as well as kinematic restrictions imposed by the surrounding tissues (Schiavone et al., 2014). However, while the high stresses of stent_{CAD} in the intima are limited to a range of $\sigma_{vM}=0.2$ to 1.6 MPa, stent_{CAD/L-PBF} and stent_{L-PBF} further induce a high fraction of intimal stresses in a range of $\sigma_{vM}=1.6$ to 4.0 MPa (Fig. 7A). The increased arterial stresses induced by stent_{CAD/L-PBF} and stent_{L-PBF} are attributed to their increased stent-to-artery ratio/overstretching of the artery due to the greater strut thickness compared with Stent_{CAD}. After stent recoil, the stresses in the intima decrease so that the majority of the intima is subjected to stresses of less $\sigma_{vM}<0.3$ MPa for all three stent models (Fig. 7B).

Thus, compared to the stress values at maximum stent expansion, the maximum and mean von Mises stress are reduced by 66%–70% and by 86%–91% in the plaque and the intima, respectively, for all three stent models (Table 4b). Using the same arterial model as in this study, Wei et al. (2019) found comparable maximal stresses in the plaque of $\sigma_{vM}=2.6$ to 5.1 MPa and in the intima of $\sigma_{vM}=0.27$ to 1.25 MPa following the expansion and recoil of various stents, thus supporting the principle plausibility of the values determined in the present study. The findings of this study, therefore, suggest that the L-PBF stent may exhibit a comparable ISR risk to that of conventionally manufactured stents. However, regarding the process-related irregularities, protruding features from the surface of stent $_{L-PBF}$ might puncture and thus damage the artery. Therefore, regardless of the arterial stress values presented here, an improvement in the quality and surface condition of L-PBF stents should be sought.

Compared to $\operatorname{stent}_{CAD}$, $\operatorname{stent}_{L-PBF}$ and $\operatorname{stent}_{CAD/L-PBF}$ induce distinctly higher maximum stresses and higher volume stresses ($\sigma_{vM}>0.2$ MPa) within the plaque and the intima (see Table 4, Fig. 7). Specifically, $\operatorname{stent}_{CAD}$ induces approximately 40% and 60% lower stresses in the plaque and intima, respectively, compared to $\operatorname{stent}_{L-PBF}$. This can be attributed to the reduced stent-to-artery ratio as well as the smaller strut thicknesses of $\operatorname{stent}_{CAD}$ compared with $\operatorname{stent}_{L-PBF}$. Thus, for conventionally manufactured stents, among others, Zahedmanesh and Lally (2009) found that stents with a strut thickness of $t_{strut}=50~\mu m$ induced 23% lower maximal arterial stresses compared to the same stent with a strut thickness of $t_{strut}=140~\mu m$. Therefore, it can be concluded that an evaluation of L-PBF stent-artery interaction based on the intended stent CAD models is not appropriate as it underestimates the L-PBF stent induced arterial stresses.

Stent $_{CAD/I-PBF}$ induces comparable maximum and mean stresses in plaque at maximum stent expansion as $stent_{L-PBF}$ with a deviation of only 1-3%. However, the maximum stresses in the intima at maximum stent expansion induced by stent_{CAD/L-PBF} are increased by 14% compared to $stent_{L-PBF}$. Moreover, after stent recoil, the maximum and mean stresses in the plaque and intima are increased by 12-19% and 34–37%, respectively. Thus, although $stent_{CAD/L-PBF}$ and stent_{L-PBF} exhibit similar stent-to-artery ratios, $\mathsf{stent}_{CAD/L-PBF}$ is not capable of accurately predicting the L-PBF stent-induced stresses. In contrast to $\text{stent}_{CAD/L-PBF}$, the struts of stent_{L-PBF} are not homogeneous and rod-shaped, but are composed of a variety of stacked melt pools resulting in inhomogeneous struts with variable cross-sections. Pronounced geometric irregularities, such as locally reduced strut diameters, might therefore lead to a reduction in the local geometric stiffness of stent_{L-PBF}. Since the struts of stent_{CAD/L-PBF} were homogeneously increased to the mean diameter of $stent_{L-PBF}$, $stent_{CAD/L-PBF}$ exhibit overall increased geometric stiffness and thus increase the stent induced arterial stresses.

3.3. Stent strain distribution at maximum stent expansion

Fig. 8 shows the contour plot of the equivalent plastic strain $\bar{\epsilon}^{pl}$ of the respective stent model in the maximally expanded state. The equivalent plastic strain ($\bar{\epsilon}^{pl}$) distribution is similar to that of free stent expansion (Wiesent et al., 2020), with strains increasing towards the stent spikes and nodes between the inclined and longitudinal struts. Unlike stent_{CAD} and stent_{CAD/L-PBF}, stent_{L-PBF} shows an inhomogeneous strain distribution with local, potentially critical, strain concentrations in the area of pronounced geometrical irregularities, such as locally reduced strut diameters and strut waviness.

With maximum equivalent plastic strains of $\bar{e}^{pl} \approx 0.68$ and $\bar{e}^{pl} \approx 1.18$, respectively, stent $_{CAD/L-PBF}$ and stent $_{L-PBF}$ exhibit significantly increased equivalent plastic strains compared to stent $_{CAD}$, which has a maximum equivalent plastic strains of $\bar{e}^{pl} \approx 0.52$ at maximum stent expansion. The increased equivalent plastic strains of stent $_{CAD/L-PBF}$ and stent $_{L-PBF}$ are attributed to the increased strut thickness and thus the increased geometrically induced stiffness of the struts against

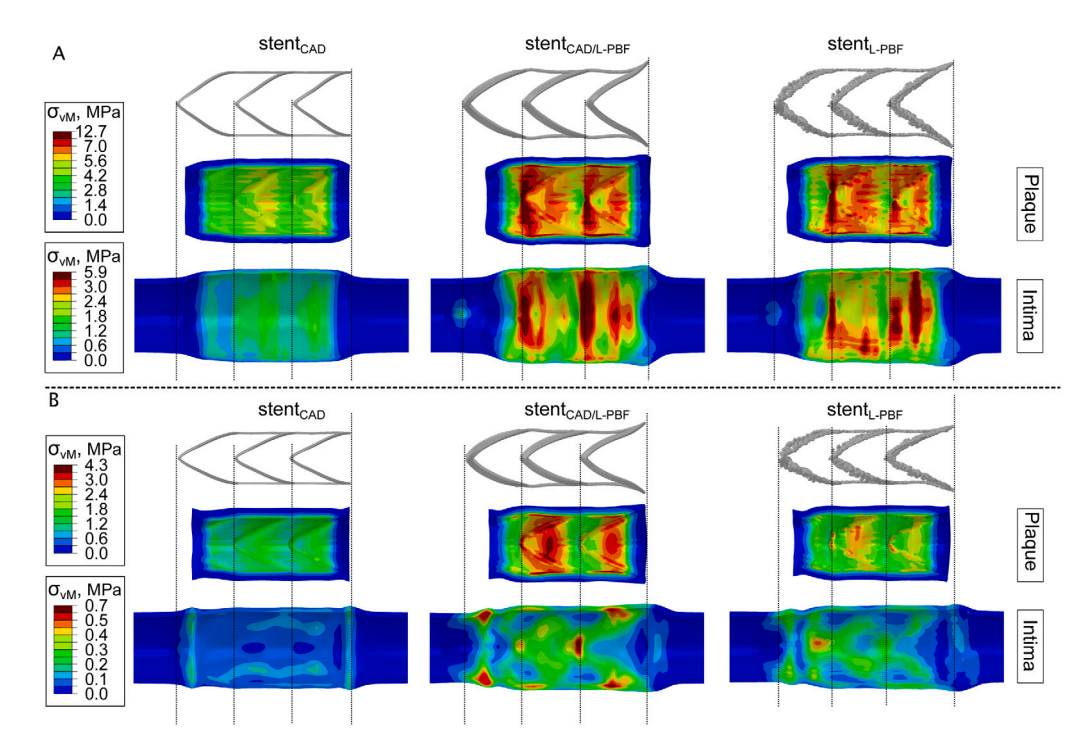


Fig. 6. Contour plot of the von Mises stress (σ_{vM}) within the plaque and the intima resulting from stent expansion A: at maximum stent expansion and B: after recoil of stent_{CAD}, stent_{CAD/L-PBF} and stent_{L-PBF} (from left to right). The stresses in the media and adventitia are negligible compared to those of the intima and plaque, so visualization of their stress distribution is omitted. Note the different legends in the subfigures A and B as well as the additionally different legends for the plaque and the intima.

Table 4

Maximum and mean values of von Mises stress ($\sigma_{vM,max}$, $\bar{\sigma}_{vM}$) in the plaque and the individual layers of the healthy arterial wall within the stenosed part of the artery after expansion of each respective stent model.

(a) Von Mises st	ress at maximum stent exp	pansion				
	$stent_{CAD}$		$stent_{CAD/L-PBF}$		$stent_{L-PBF}$, MPa	
	$\sigma_{vM,max}$, MPa	$\bar{\sigma}_{vM}$ ± SD, MPa	$\sigma_{vM.max}$, MPa	$\bar{\sigma}_{vM} \pm \text{SD, MPa}$	$\sigma_{vM,max}$, MPa	$\bar{\sigma}_{vM}$ ± SD, MPa
Plaque	7.074	1.122 ± 1.298	12.665	1.509 ± 1.815	12.441	1.478 ± 1.767
Intima	2.057	0.656 ± 0.463	5.940	1.335 ± 1.000	5.170	1.289 ± 0.940
Media	0.034	0.016 ± 0.007	0.065	0.021 ± 0.010	0.059	0.021 ± 0.010
Adventitia	0.015	0.007 ± 0.003	0.025	0.010 ± 0.004	0.023	0.010 ± 0.004
(b) Von Mises st	ress after stent recoil					
	$stent_{CAD}$		$stent_{CAD/L-PBF}$		$stent_{L-PBF}$, MPa	
	$\sigma_{vM,max}$, MPa	$\bar{\sigma}_{vM} \pm \text{SD, MPa}$	$\sigma_{vM.max}$, MPa	$\bar{\sigma}_{vM} \pm \text{SD, MPa}$	$\sigma_{vM,max}$, MPa	$\bar{\sigma}_{vM}$ ± SD, MPa
Plaque	2.067	0.342 ± 0.348	3.98	0.601 ± 0.665	3.55	0.501 ± 0.533
Intima	0.219	0.067 ± 0.028	0.668	0.176 ± 0.105	0.496	0.130 ± 0.069
Media	0.016	0.005 ± 0.002	0.026	0.009 ± 0.004	0.024	0.008 ± 0.003
Adventitia	0.008	$0.003 \pm < 0.001$	0.011	0.005 ± 0.002	0.010	0.005 ± 0.001

stent expansion. As indicated before, for $stent_{L-PBF}$, further strain concentrations are observed at locally pronounced geometric irregularities (notches, reduced strut diameters). In the literature, elongations at fracture of $\epsilon_F \approx 0.25$ have been reported for individual L-PBF 316L struts with a diameter of $D_{strut} \approx 200 \ \mu m$ (Gümrük and Mines, 2013). Thus, the observed locally increased equivalent plastic strains of $\bar{\epsilon}^{pl} > 0.25$ within stent_{CAD/L-PBF} and stent_{L-PBF} should be considered critical in terms of their structural integrity in the worst-case scenario (Fig. 8) (Gümrük and Mines, 2013). Moreover, morphological irregularities, such as notch-like reductions in strut diameter, wavy strut shapes, and pores might also promote stent failure after longterm use due to high-cycle fatigue. After strut fracture, protruding strut fragments can either cause ISR due to local mechanical irritation of the vessel wall or promote thrombosis due to unfavorable changes in hemodynamics (Adlakha et al., 2010). Therefore, further studies into the failure mechanism of L-PBF stents are required.

The intended $stent_{CAD}$ was unable to predict plastic strains within the L-PBF stent. Upon modifying the original CAD stent model to

account for the increased strut diameters of L-PBF stents, however, stent $_{CAD/L-PBF}$ was able to predict a strain distribution (more) comparable to that of stent $_{L-PBF}$. However, as expected, the additional local strain concentration in areas of particularly pronounced irregularities of stent $_{L-PBF}$ could not be predicted by stent $_{CAD/L-PBF}$.

3.4. Limitations and scope for future research

There are a number of modeling assumptions made in this work that merit further discussion. In this study, a simplified arterial model with a symmetric plaque is used, neglecting the anisotropic material behavior of the artery, arterial damage and healing processes, and natural morphological variations of the artery (e.g. local changes in arterial cross-section and curvature). Due to the comparative nature of this study, a simplified straight arterial model was deliberately chosen to minimize any additional influence factors on stent-induced arterial stresses and thus to focus only on the influence of stent morphological irregularities on the stent-artery interaction. In later studies, the impact

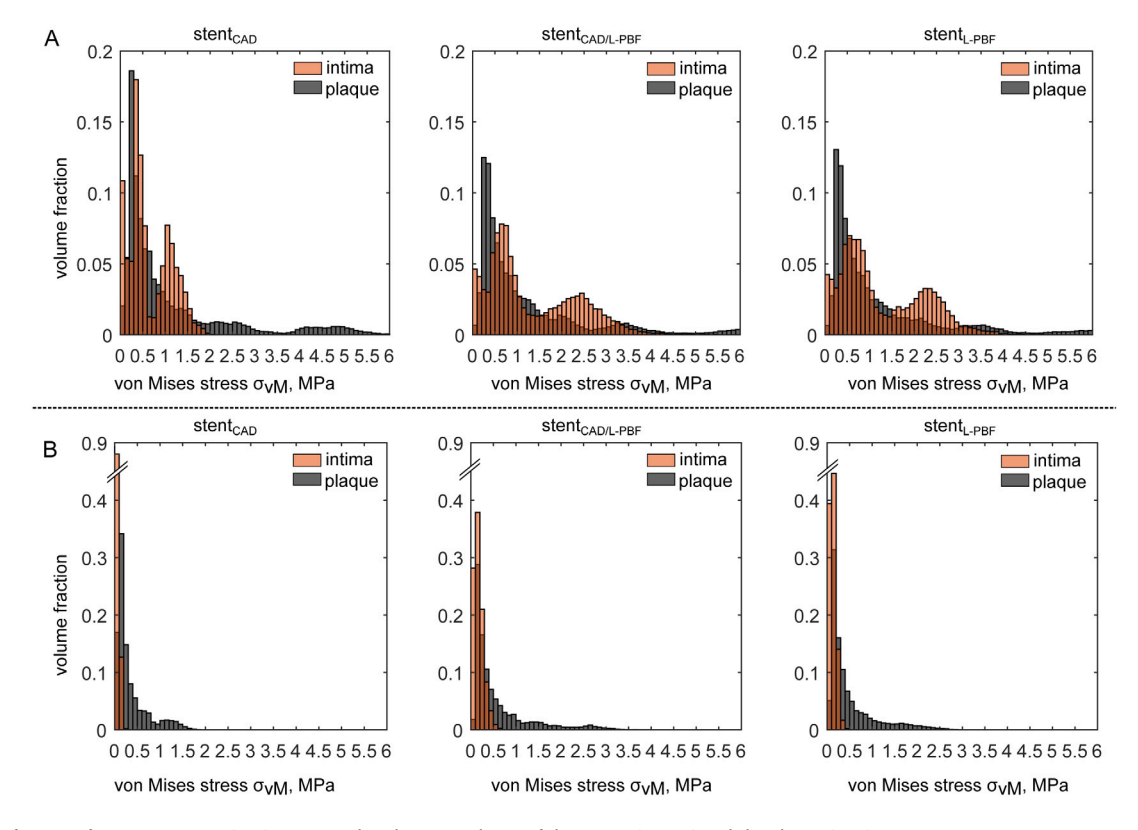


Fig. 7. Volume fraction of von Mises stress (σ_{vM}) ranges within the stenosed part of the intima (orange) and the plaque (gray) A: at maximum stent expansion and B: after recoil of stent_{CAD}, stent_{CAD/L-PBF} and stent_{L-PBF} (from left to right).

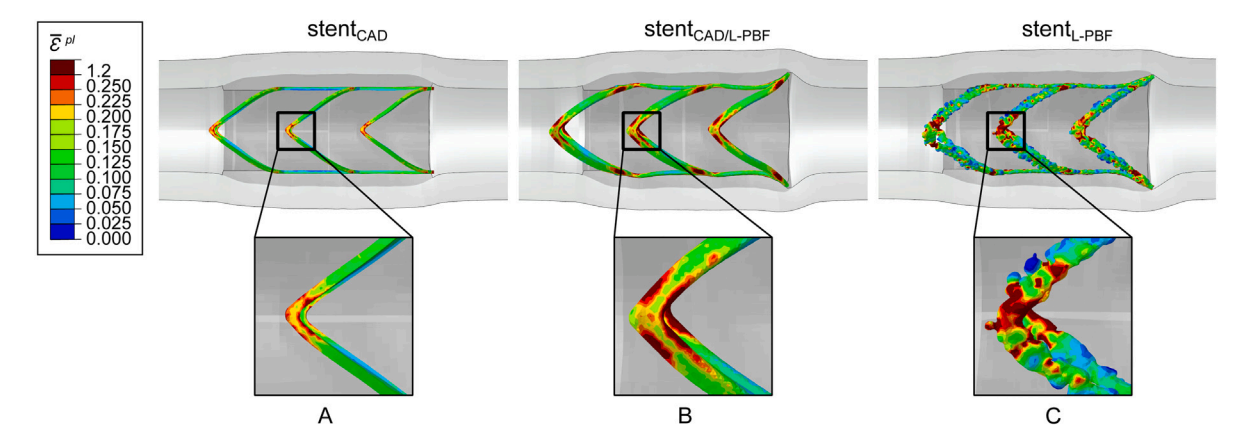


Fig. 8. Contour plot of the equivalent plastic strain (\bar{e}^{pl}) within each stent model at the maximum expanded state within the stenosed artery. A: $\operatorname{stent}_{CAD}$, B: $\operatorname{stent}_{CAD/L-PBF}$ and C: $\operatorname{stent}_{L-PBF}$. The upper contour limit was chosen to highlight potential locations of failure where \bar{e}^{pl} exceeds 0.25, following tensile test results on individual L-PBF 316L struts from Gümrük and Mines (2013). The arterial wall is illustrated in gray and the plaque in dark gray.

of morphological artery variations, bifurcations, and patient-specific arteries should be investigated. The approximation of the arterial material as isotropic can be justified because the predominant mechanical properties of the artery during stent expansion are the circumferential properties (Zahedmanesh and Lally, 2009). Because arterial damage and healing process were not considered within this study, it is difficult to assess whether local high stress concentrations, even in small areas, should be considered critical or negligible with respect to the development of ISR. In this context, further numerical/experimental studies should be conducted to identify critical threshold for geometrical irregularities with respect to the stent-artery interaction.

The assessment of the impact of the geometrical irregularities of the L-PBF stent on the arterial stresses is based only on a single L-PBF stent configuration. Different stent designs, L-PBF process parameters, raw materials, and post-processing steps have been shown to result in different surface qualities, mechanical properties, and thus different stent expansion behavior (Finazzi et al., 2020; Wiesent et al., 2020). The methodology presented here could be further used in a more comprehensive study on a larger number of L-PBF stents in combination with statistical methods to allow a more general assessment of the interaction of L-PBF stents with arteries. In this context, stent failure/fatigue should be included in these investigation to asses the impact of stent failure on the arterial tissue. The results of this study motivate future research to improve the manufacturing and post-processing parameters to reduce geometrical irregularities, to develop/optimize new stent designs considering unavoidable irregularities, and to identify critical thresholds of geometrical irregularities for potential stent application.

This study is based on a purely structural analysis of the L-PBF stent-artery interaction. Therefore, no information regarding the impact of the stent geometrical irregularities on hemodynamics can be

provided. Protruding morphological irregularities associated with L-PBF might negatively impact the blood flow. However, by enabling customized stents, the stent-artery conformity could also be improved, thus potentially reducing the risk of unwanted turbulence in the blood flow and reducing the associated risk of thrombosis (Wu et al., 2007). Therefore, combined structural-mechanical and fluid-dynamic studies should be performed on patient-specific L-PBF stents, which could provide indications of the full potential of L-PBF stents.

A further limitation of this work is the lack of validation of arterial stresses. Use of a validated arterial model and comparison of the arterial stresses with literature data from conventional stents suggests that the simulations presented here are reasonable, but experimental validation would still be beneficial.

The analysis of stent-artery interaction presented here was performed at an early stage of L-PBF stent research, and a significant improvement of stent-artery interaction with further improvement of L-PBF processes and the development of special L-PBF stent designs is expected. Nevertheless, we have shown that the basic computational methods for stent-artery interaction of conventional stents (e.g. with respect to the impact of the primary stent design) can also be transferred to L-PBF stents. In addition, the L-PBF stent was found to induce increased stresses in the plaque but did not result in a critical increase in intimal stresses. This indicates, that the use of L-PBF stents might be possible in principle in the future if the irregularities can be reduced to a minimum. However, further numerical and experimental studies are needed concerning the stent-artery interaction, biocompatibility, and fatigue resistance of L-PBF stents.

4. Conclusions

To establish L-PBF as a manufacturing method for stents, it is essential to identify critical process-related factors that influence stent-artery interaction. Three such factors were investigated in this study: stent design, strut thickness, and geometrical irregularities associated with L-PBF (e.g. protruding features from the stent surface, and local notches). The following conclusions can be drawn:

- Arterial stresses are primarily governed by the overarching stent design (topology), and new stent designs need to be developed/optimized for L-PBF. L-PBF stent designs should meet the requirements for manufacturability by L-PBF, expandability by balloon catheter, and adequate stent-artery interaction (e.g., subcritical stent-induced stresses and sufficient area coverage).
- Due to differences in morphology of an L-PBF stent from its intended stent design, determination of arterial stresses based on the intended stent CAD model results in underestimation of stress in the plaque and intima by approximately 40% and 60%, respectively.
- 3. The arterial stresses induced by the L-PBF stent are influenced by both the increased strut thickness and geometric process irregularities. These affect not only the stent-to-artery ratio but also the local geometric stiffness of the stent. Due to missing consideration of the stiffness-reducing effect of geometric irregularities, a mere increase in strut thickness leads to an overestimation of L-PBF stent-induced arterial stresses (max and mean) by about 12–37%.
- 4. In the stent itself, the L-PBF process-related geometrical irregularities lead to local strain peaks during expansion, which can potentially cause strut fracture and thus induced vascular damage.
- 5. Improvements in the L-PBF process or the use of L-PBF equipment specifically optimized for filigree lattice structures, as well as improvements in the post-processing of L-PBF stents, are imperative to establish L-PBF as an alternative manufacturing process for cardiovascular stents.

The findings from this work motivate future experimental/numerical studies to reduce geometric irregularities and to quantify threshold values of critical geometric irregularities with regards to both the stent-artery interaction and the mechanical behavior of the L-PBF stent.

CRediT authorship contribution statement

Lisa Wiesent: Conceptualization, Formal analysis, Methodology, Software, Validation, Visualization, Writing – original draft. **Ashley Spear:** Conceptualization, Funding acquisition, Project administration, Supervision, Writing – review & editing. **Aida Nonn:** Conceptualization, Project administration, Resources, Supervision, Writing – review & editing.

Declaration of competing interest

The authors declare that they have no known competing financial interests or personal relationships that could have appeared to influence the work reported in this paper.

Acknowledgments

This work was performed within a Fulbright doctoral fellowship. It was further supported by the Bayerische Forschungsstiftung, Germany ['NewGen-Stent': grant number AZ-1221-16], the Bayarian Academic Forum (BayWISS) - Doctoral Consortium 'Health Research', Germany, and by the National Science Foundation, United States under Grant No. CMMI-1752400. Further, the support and resources from the Center for High Performance Computing at the University of Utah, as well as from the Regensburg Center of Biomedical Engineering (RCBE) for providing μ -CT which is supported by the Deutsche Forschungsgemeinschaft (DFG), Germany [grand number INST 102/11-1 FUGG], are gratefully acknowledged. Special thanks also goes to Ulrich Schultheiß for conducting stent post-processing treatment and to Philipp Lulla for providing the stent.

References

- Adlakha, S., Sheikh, M., Wu, J., Burket, M.W., Pandya, U., Colyer, W., Eltahawy, E., Cooper, C.J., 2010. Stent fracture in the coronary and peripheral arteries. J. Interv. Cardiol. 23 (4), 411–419. http://dx.doi.org/10.1111/j.1540-8183.2010.00567.x.
- Auricchio, F., Conti, M., De Beule, M., De Santis, G., Verhegghe, B., 2011. Carotid artery stenting simulation: From patient-specific images to finite element analysis. Med. Eng. Phys. 33 (3), 281–289. http://dx.doi.org/10.1016/j.medengphy.2010.10.011.
- Balossino, R., Gervaso, F., Migliavacca, F., Dubini, G., 2008. Effects of different stent designs on local hemodynamics in stented arteries. J. Biomech. 41 (5), 1053–1061. http://dx.doi.org/10.1016/j.jbiomech.2007.12.005.
- Campoli, G., Borleffs, M.S.S., Amin Yavari, S., Wauthle, R., Weinans, H., Zadpoor, A.A.A., 2013. Mechanical properties of open-cell metallic biomaterials manufactured using additive manufacturing. Mater. Des. 49, 957–965. http://dx.doi.org/10.1016/j.matdes.2013.01.071, URL: https://linkinghub.elsevier.com/retrieve/pii/S0261306913000940.
- Capelli, C., Gervaso, F., Petrini, L., Dubini, G., Migliavacca, F., 2009. Assessment of tissue prolapse after balloon-expandable stenting: Influence of stent cell geometry. Med. Eng. Phys. 31, 441–447. http://dx.doi.org/10.1016/j.medengphy.2008.11. 002.
- Chen, H.Y., Hermiller, J., Sinha, A.K., Sturek, M., Zhu, L., Kassab, G.S., 2009. Effects of stent sizing on endothelial and vessel wall stress: Potential mechanisms for instent restenosis. J. Appl. Physiol. 106 (5), 1686–1691. http://dx.doi.org/10.1152/ japplphysiol.91519.2008.
- Conway, C., McGarry, J.P., McHugh, P.E., 2014. Modelling of atherosclerotic plaque for use in a computational test-bed for stent angioplasty. Ann. Biomed. Eng. 42 (12), 2425–2439. http://dx.doi.org/10.1007/s10439-014-1107-4.
- Conway, C., Sharif, F., McGarry, J.P., McHugh, P.E., 2012. A computational test-bed to assess coronary stent implantation mechanics using a population-specific approach. Cardiovasc. Eng. Technol. 3 (4), 374–387. http://dx.doi.org/10.1007/s13239-012-0104-8.
- Dassault Systemes, 2013. 6.13 Documentation (Abaqus), 2013, Abaqus User's Guide. p. 1138.

- De Beule, M., Mortier, P., Carlier, S.G., Verhegghe, B., Van Impe, R., Verdonck, P., 2008. Realistic finite element-based stent design: The impact of balloon folding. J. Biomech. 41 (2), 383–389. http://dx.doi.org/10.1016/j.jbjomech.2007.08.014.
- Demir, A.G., Previtali, B., 2017. Additive manufacturing of cardiovascular CoCr stents by selective laser melting. Mater. Des. 119, 338–350. http://dx.doi.org/10.1016/j. matdes.2017.01.091.
- Djukic, T., Saveljic, I., Pelosi, G., Parodi, O., Filipovic, N., 2019. Numerical simulation of stent deployment within patient-specific artery and its validation against clinical data. Comput. Methods Programs Biomed. 175, 121–127. http://dx.doi.org/10. 1016/j.cmpb.2019.04.005.
- Dong, Z., Zhang, X., Shi, W., Zhou, H., Lei, H., Liang, J., 2018. Study of size effect on microstructure and mechanical properties of AlSi10Mg samples made by selective laser melting. Materials 11 (12), http://dx.doi.org/10.3390/ma11122463.
- Finazzi, V., Demir, A.G., Biffi, C.A., Chiastra, C., Migliavacca, F., Petrini, L., Previtali, B., 2019. Design rules for producing cardiovascular stents by selective laser melting: Geometrical constraints and opportunities. Procedia Struct. Integr. 15, 16–23. http://dx.doi.org/10.1016/j.prostr.2019.07.004.
- Finazzi, V., Demir, A.G., Biffi, C.A., Migliavacca, F., Petrini, L., Previtali, B., 2020. Design and functional testing of a novel balloon-expandable cardiovascular stent in CoCr alloy produced by selective laser melting. J. Manuf. Process. 55 (February), 161–173. http://dx.doi.org/10.1016/j.jmapro.2020.03.060.
- Gonzalez, F.J.Q., Nuno, N., 2016. Finite element modeling of manufacturing irregularities of porous materials. Biomater. Biomech. Bioeng. 3 (1), 1–14. http://dx.doi.org/10.12989/bme.2016.3.1.001, URL: http://koreascience.or.kr/journal/view.jsp?kj=E1TPEG{&p}v=2016{&}vnc=v3n1{&}sp=1.
- Grewe, P.H., Deneke, T., Machraoui, A., 2000. Acute and chronic tissue response to coronary stent implantation: Pathologic findings in human specimen. J. Am. Coll. Cardiol. 35 (1), http://dx.doi.org/10.1016/S0735-1097(99)00486-6.
- Grogan, J.A., Leen, S.B., McHugh, P.E., 2012. Comparing coronary stent material performance on a common geometric platform through simulated bench testing. J. Mech. Behav. Biomed. Mater. 12, 129–138. http://dx.doi.org/10.1016/j.jmbbm. 2012.02.013.
- Gümrük, R., Mines, R.A.W., 2013. Compressive behaviour of stainless steel micro-lattice structures. Int. J. Mech. Sci. 68, 125–139. http://dx.doi.org/10.1016/j.ijmecsci.2013.01.006, URL: http://www.sciencedirect.com/science/article/pii/S0020740313000118. https://linkinghub.elsevier.com/retrieve/pii/S0020740313000118.
- Gyöngyösi, M., Yang, P., Khorsand, A., Glogar, D., Gyo, M., Gyöngyösi, M., Yang, P., Khorsand, A., Glogar, D., 2000. Longitudinal straightening effect of stents is an additional predictor for major adverse cardiac events. J. Am. Coll. Cardiol. 35 (6), 1580–1589. http://dx.doi.org/10.1016/S0735-1097(00)00570-2.
- Hasgall, P., Di Gennaro, F., Baumgartner, C., Neufeld, E., Lloyd, B., Gosselin, M., Payne, D., Klingenböck, A., Kuster, N., 2018. IT'lS database for thermal and electromagnetic parameters of biological tissues. http://dx.doi.org/10.13099/VIP21000-04-0, URL: https://itis.swiss/virtual-population/tissue-properties/database/density/.
- He, R., Zhao, L.G., Silberschmidt, V.V., Liu, Y., Vogt, F., 2020. Finite element evaluation of artery damage in deployment of polymeric stent with pre- and post-dilation. Biomech. Model. Mechanobiol. 19 (1), 47–60. http://dx.doi.org/10.1007/s10237-019-01194-6, URL: http://link.springer.com/10.1007/s10237-019-01194-6.
- Holzapfel, G.A., Sommer, G., Gasser, C.T., Regitnig, P., 2005. Determination of layer-specific mechanical properties of human coronary arteries with nonatherosclerotic intimal thickening and related constitutive modeling. Am. J. Physiol. Heart Circ. Physiol. 289 (5 58-5), 2048–2058. http://dx.doi.org/10.1152/ajpheart.00934.2004.
- Htay, T., Liu, M.W., 2005. Drug-eluting stent: A review and update. Vasc. Health Risk Manage. 1 (4), 263–276.
- Hufenbach, J., Sander, J., Kochta, F., Pilz, S., Voss, A., Kühn, U., Gebert, A., 2020. Effect of selective laser melting on microstructure, mechanical, and corrosion properties of biodegradable FeMnCS for implant applications. Adv. Energy Mater. 2000182 (10), 1–8. http://dx.doi.org/10.1002/adem.202000182, URL: https://onlinelibrary.wiley.com/doi/10.1002/adem.202000182.
- Ijsselmuiden, A.J.J., Serruys, P.W., Scholte, A., Kiemeneij, F., Slagboom, T., Wieken, L.R.V., Tangelder, G.J., Laarman, G.J., 2003. Direct coronary stent implantation does not reduce the incidence of in-stent restenosis or major adverse cardiac events: Six month results of a randomized trial. Eur. Heart J. 24 (5), 421–429. http://dx.doi.org/10.1016/S0195-668X(02)00701-7.
- Karamooz Ravari, M.R., Kadkhodaei, M., 2015. A computationally efficient modeling approach for predicting mechanical behavior of cellular lattice structures. J. Mater. Eng. Perform. 24 (1), 245–252. http://dx.doi.org/10.1007/s11665-014-1281-4.
- Kastrati, A., Mehilli, J., Dirschinger, J., Pache, J., Ulm, K., Schühlen, H., Seyfarth, M., Schmitt, C., Blasini, R., Neumann, F.-J., Schömig, A., 2001. Restenosis after coronary placement of various stent types. Am. J. Cardiol. 87 (1), 34–39. http://dx.doi.org/10.1016/S0002-9149(00)01268-6, URL: https://linkinghub.elsevier.com/retrieve/pii/S0002914900012686.

- Kim, M.S., Dean, L.S., 2011. In-stent restenosis. Cardiovasc. Ther. 29 (3), 190–198. http://dx.doi.org/10.1111/j.1755-5922.2010.00155.x.
- Kurata, N., Iida, O., Shiraki, T., Fujita, M., Masuda, M., Okamoto, S., Ishihara, T., Nanto, K., Kanda, T., Sunaga, A., Tsujimura, T., Takahara, M., Mano, T., 2018. Impact of stent-to-vessel diameter ratio on restenosis in the superficial femoral artery after endovascular therapy. Circ. J. 82 (5), 1412–1417. http://dx.doi.org/10.1253/circj.CJ-17-0726, URL: https://www.jstage.jst.go.jp/article/circj/82/5/82{_}CJ-17-0726/_article.
- Lapp, H., 2019. Das Herzkatheterbuch. Georg Thieme Verlag, Stuttgart, http://dx.doi. org/10.1055/b-006-160381.
- Latib, A., Colombo, A., 2008. Bifurcation disease: What do we know, what should we do? JACC Cardiovasc. Interv. 1 (3), 218–226. http://dx.doi.org/10.1016/j.jcin. 2007.12.008.
- Lei, H., Li, C., Meng, J., Zhou, H., Liu, Y., Zhang, X., Wang, P., Fang, D., 2019. Evaluation of compressive properties of SLM-fabricated multi-layer lattice structures by experimental test and μ-CT-based finite element analysis. Mater. Des. 169, 107685. http://dx.doi.org/10.1016/j.matdes.2019.107685, URL: https://linkinghub.elsevier.com/retrieve/pii/S0264127519301224.
- Lepor, N.E., Madyoon, H., Kereiakes, D.J., 2002. Effective and efficient strategies for coronary revascularization in the drug-eluting stent era. Rev. Cardiovasc. Med. 3 Suppl 5, S38–50.
- Liu, L., Kamm, P., García-Moreno, F., Banhart, J., Pasini, D., 2017. Elastic and failure response of imperfect three-dimensional metallic lattices: The role of geometric defects induced by selective laser melting. J. Mech. Phys. Solids 107, 160–184. http://dx.doi.org/10.1016/j.jmps.2017.07.003.
- Loree, H.M., Grodzinsky, A.J., Park, S.Y., Gibson, L.J., Lee, R.T., 1994. Static circumferential tangential modulus tissue. J. Biomech. 27 (2), 195–204.
- Mahmoud, D., Elbestawi, M., 2017. Lattice structures and functionally graded materials applications in additive manufacturing of orthopedic implants: A review. J. Manuf. Mater. Process. 1 (2), 13. http://dx.doi.org/10.3390/jmmp1020013, URL: http://www.mdpi.com/2504-4494/1/2/13.
- Morlacchi, S., Colleoni, S.G., Cárdenes, R., Chiastra, C., Diez, J.L., Larrabide, I., Migliavacca, F., 2013. Patient-specific simulations of stenting procedures in coronary bifurcations: Two clinical cases. Med. Eng. Phys. 35 (9), 1272–1281. http://dx.doi.org/10.1016/j.medengphy.2013.01.007, URL: http://dx.doi.org/10.1016/j.medengphy.2013.01.007.
- Nandishwarsteel, 2010. ASME SA 240 stainless steel 316/ 316L sheets and plates. URL: https://www.nandishwarsteel.com/stainless-steel-316-316l-sheets-plates.html.
- Ogden, R.W., 1972. Large deformation isotropic elasticity: On the correlation of theory and experiment for compressible rubberlike solids. Proc. R. Soc. Lond. Ser. A Math. Phys. Eng. Sci. 328 (1575), 567–583. http://dx.doi.org/10.1098/rspa.1972.0096, URL: https://royalsocietypublishing.org/doi/10.1098/rspa.1972.0096.
- Parthasarathy, J., Starly, B., Raman, S., 2011. A design for the additive manufacture of functionally graded porous structures with tailored mechanical properties for biomedical applications. J. Manuf. Process. 13 (2), 160–170. http://dx.doi.org/ 10.1016/j.jmapro.2011.01.004, URL: https://linkinghub.elsevier.com/retrieve/pii/ S1526612511000053.
- Prendergast, P.J., Lally, C., Daly, S., Reid, A.J., Lee, T.C., Quinn, D., Dolan, F., 2003. Analysis of prolapse in cardiovascular stents: A constitutive equation for vascular tissue and finite-element modelling. J. Biomech. Eng. 125 (5), 692–699. http://dx.doi.org/10.1115/1.1613674.
- Rahdert, D.A., Sweet, W.L., Tio, F.O., Janicki, C., Duggan, D.M., 1999. Measurement of density and calcium in human atherosclerotic plaque and implications for arterial brachytherapy. Cardiovasc. Radiat. Med. 1 (4), 358–367. http://dx.doi.org/10. 1016/S1522-1865(00)00030-5, URL: https://linkinghub.elsevier.com/retrieve/pii/ S1522186500000305.
- Schiavone, A., Zhao, L.G., Abdel-Wahab, A.A., 2014. Effects of material, coating, design and plaque composition on stent deployment inside a stenotic artery Finite element simulation. Mater. Sci. Eng. C 42, 479–488. http://dx.doi.org/10.1016/j.msec.2014.05.057.
- Serruys, P.W., Kutryk, M.J.B., Ong, A.T.L., 2006. Coronary-artery stents. N. Engl. J. Med. 354 (5), 483–495. http://dx.doi.org/10.1056/NEJMra051091.
- Stone, P.H., Coskun, A.U., Kinlay, S., Clark, M.E., Sonka, M., Wahle, A., Ilegbusi, O.J., Yeghiazarians, Y., Popma, J.J., Orav, J., Kuntz, R.E., Feldman, C.L., 2003. Effect of endothelial shear stress on the progression of coronary artery disease, vascular remodeling, and in-stent restenosis in humans: In vivo 6-month follow-up study. Circulation 108 (4), 438–444. http://dx.doi.org/10.1161/01.CIR. 0000080882.35274.AD.
- Timmins, L.H., Meyer, C.A., Moreno, M.R., Moore, J.E., 2008. Mechanical modeling of stents deployed in tapered arteries. Ann. Biomed. Eng. 36 (12), 2042–2050. http://dx.doi.org/10.1007/s10439-008-9582-0.
- Timmins, L.H., Miller, M.W., Clubb, F.J., Moore, J.E., 2011. Increased artery wall stress post-stenting leads to greater intimal thickening. Lab. Invest. 91 (6), 955–967. http://dx.doi.org/10.1038/labinvest.2011.57.

- Wei, L., Leo, H.L., Chen, Q., Li, Z., 2019. Structural and hemodynamic analyses of different stent structures in curved and stenotic coronary artery. Front. Bioeng. Biotechnol. 7 (December), 1–13. http://dx.doi.org/10.3389/fbioe.2019.00366.
- Wiesent, L., Schultheiß, U., Lulla, P., Noster, U., Schratzenstaller, T., Schmid, C., Nonn, A., Spear, A., 2020. Computational analysis of the effects of geometric irregularities and post-processing steps on the mechanical behavior of additively manufactured 316L stainless steel stents. PLoS One 15 (12), e0244463. http://dx.doi.org/10.1371/journal.pone.0244463.
- Wiesent, L., Schultheiß, U., Schmid, C., Schratzenstaller, T., Nonn, A., 2019. Experimentally validated simulation of coronary stents considering different dogboning ratios and asymmetric stent positioning. PLoS One 14 (10), 1–25. http://dx.doi.org/10.1371/journal.pone.0224026.
- Wu, W., Qi, M., Liu, X.P., Yang, D.Z., Wang, W.Q., 2007. Delivery and release of nitinol stent in carotid artery and their interactions: A finite element analysis. J. Biomech. 40 (13), 3034–3040. http://dx.doi.org/10.1016/j.jbiomech.2007.02.024.
- Zahedmanesh, H., Lally, C., 2009. Determination of the influence of stent strut thickness using the finite element method: Implications for vascular injury and in-stent restenosis. Med. Biol. Eng. Comput. 47 (4), 385–393. http://dx.doi.org/10.1007/s11517-009-0432-5.